



# Multifunctional porous silicon nanoparticles for cancer theranostics



Chang-Fang Wang<sup>a,1</sup>, Mirkka P. Sarparanta<sup>b,1,2</sup>, Ermei M. Mäkilä<sup>a,c</sup>,  
Maija L.K. Hyvönen<sup>d</sup>, Pirjo M. Laakkonen<sup>d</sup>, Jarno J. Salonen<sup>c</sup>, Jouni T. Hirvonen<sup>a</sup>,  
Anu J. Airaksinen<sup>b,\*\*</sup>, Hélder A. Santos<sup>a,\*</sup>

<sup>a</sup> Division of Pharmaceutical Chemistry and Technology, Faculty of Pharmacy, University of Helsinki, FI-00014 Helsinki, Finland

<sup>b</sup> Laboratory of Radiochemistry, Department of Chemistry, University of Helsinki, FI-00014 Helsinki, Finland

<sup>c</sup> Laboratory of Industrial Physics, Department of Physics and Astronomy, University of Turku, FI-20014 Turku, Finland

<sup>d</sup> Research Programs Unit, Translational Cancer Biology and Institute of Biomedicine, Biomedicum Helsinki, University of Helsinki, FI-00014 Helsinki, Finland

## ARTICLE INFO

### Article history:

Received 2 September 2014

Accepted 20 January 2015

Available online 11 February 2015

### Keywords:

Theranostics

Targeting drug delivery

Surface multifunctionalization

Porous silicon nanoparticles

Cancer therapy

## ABSTRACT

Nanomaterials provide a unique platform for the development of theranostic systems that combine diagnostic imaging modalities with a therapeutic payload in a single probe. In this work, dual-labeled iRGD-modified multifunctional porous silicon nanoparticles (PSi NPs) were prepared from dibenzocyclooctyl (DBCO) modified PSi NPs by strain-promoted azide-alkyne cycloaddition (SPAAC) click chemistry. Hydrophobic antiangiogenic drug, sorafenib, was loaded into the modified PSi NPs to enhance the drug dissolution rate and improve cancer therapy. Radiolabeling of the developed system with <sup>111</sup>In enabled the monitoring of the *in vivo* biodistribution of the nanocarrier by single photon emission computed tomography (SPECT) in an ectopic PC3-MM2 mouse xenograft model. Fluorescent labeling with Alexa Fluor 488 was used to determine the long-term biodistribution of the nanocarrier by immunofluorescence at the tissue level *ex vivo*. Modification of the PSi NPs with an iRGD peptide enhanced the tumor uptake of the NPs when administered intravenously. After intratumoral delivery the NPs were retained in the tumor, resulting in efficient tumor growth suppression with particle-loaded sorafenib compared to the free drug. The presented multifunctional PSi NPs highlight the utility of constructing a theranostic nanosystems for simultaneous investigations of the *in vivo* behavior of the nanocarriers and their drug delivery efficiency, facilitating the selection of the most promising materials for further NP development.

© 2015 Elsevier Ltd. All rights reserved.

## 1. Introduction

Cancer is the first most common cause of death in Europe [1] and the second leading cause of death in the US [2]. For most of the cancers, earlier detection and treatment provide substantial better survival rate [1,2]. Nanocarrier-based targeted delivery of chemotherapeutic agents to the tumor can increase the local drug concentration in the tumor tissue and lower the systemic exposure, hence reducing the side effects of the drugs [3,4]. On the other hand, accurate diagnostics is a key issue for the early detection and treatment of cancer. The so-called theranostic systems, which combine diagnostic imaging with delivery of therapeutic agents, are a recent advance in the development of nanomedicines [5]. For

the development and performance evaluation of these drug delivery systems it is also very important to have the necessary imaging tools to follow the fate of the developed nanocarriers *in vivo* [6].

SPECT (Single photon emission computed tomography) detects the gamma (γ)-rays, i.e., photons resulted from the decay of radionuclides including <sup>111</sup>In, <sup>99m</sup>Tc, <sup>123</sup>I, and <sup>131</sup>I, and is in use in clinical applications [7]. Radiolabeling of the nanocarrier-based therapeutic systems with γ-emitting radionuclides can provide a highly sensitive and quantitative evaluation of their *in vivo* biodistribution. X-ray computer tomography (CT) in turn has a high spatial resolution for assessment of anatomic structure, information that is not conferred by the SPECT measurement. Combination

\* Corresponding author. Tel.: +358 2941 59661.

\*\* Corresponding author. Tel.: +358 2941 50124.

E-mail addresses: [anu.airaksinen@helsinki.fi](mailto:anu.airaksinen@helsinki.fi) (A.J. Airaksinen), [helder.santos@helsinki.fi](mailto:helder.santos@helsinki.fi) (H.A. Santos).

<sup>1</sup> These authors contributed equally to this work.

<sup>2</sup> Current address: Department of Radiology and the Program in Molecular Pharmacology & Chemistry, Memorial Sloan Kettering Cancer Center, New York, NY 10065, USA.

of SPECT and CT techniques is commonly utilized for clinical and pre-clinical applications, providing a 3-D distribution of the radiotracer with precise anatomical localization [8]. On the other hand, fluorescence dyes are widely used in biomedical research to provide an efficient, convenient and radiation-free modality for preclinical cancer imaging and research.

To meet the theranostic requirements, a single nanocarrier has to include both therapeutic payloads and imaging probes. Nanocarriers such as lipid-based liposomes, polymeric nanoparticles, carbon nanotubes, and inorganic nanosystems (e.g., gold nanoparticles, magnetic nanoparticles, and silicon/silica particles) have been widely investigated for drug delivery applications [5,9–17]. Porous silicon (PSi) displays many advantageous properties that render it as a potential theranostic vector in biomedical applications [18–25], such as high biocompatibility, capability to increase the dissolution rate of poorly water-soluble drugs [26], high drug loading capacity [27], and tunable surface chemistry [16,28,29].

Surface modification is necessary to introduce fluorophores, chelators for radiolabeling, and hydrophilic targeting moieties to modulate the properties of PSi for cancer drug delivery [16,20,29,30]. Intravenously administrated nanocarriers can be delivered to the tumor site by the enhanced permeability and retention (EPR) effect or by receptor-mediated active targeting after conjugation of targeting ligands [31]. In addition, the surface bio-functionalization of NPs will modulate the tissue distribution and elimination profiles of the nanocarriers [32,33]. Strain-promoted azide-alkyne cycloaddition (SPAAC) click reaction is an approach for the surface modification of nanomaterials for biomedical applications [34–36]. SPAAC provides several advantages, such as high selectivity, efficiency, and mild/aqueous solution reaction conditions needed [37]. iRGD is a 9-amino acid cyclic variant of RGD (Arg-Gly-Asp) peptide, identified by phage display technology as a tumor targeting and tissue penetrating peptide [38] that has been used to target nanoparticles to cancer therapy applications [39].

Intratumoral administration can provide 100% delivery of the anticancer agent to the injection site. However, conventional small drug molecules can be rapidly pumped out from the tumor into the bloodstream after intratumoral injection, due to the high pressure environment in the tumor or the proteins that exclude drugs from tumor cells and tissues [40,41]. For example, polymeric nanocarriers and cationic liposomes have been shown to increase the tumor retention of loaded drugs after intratumoral administration [40,42].

Here, dual-modality nanotheranostic PSi NPs were prepared by conjugating 1,4,7,10-tetraazacyclododecane-N,N',N'',N'''-tetraacetic acid (DOTA), Alexa Fluor 488 and the peptide iRGD on the surface of the particles using the SPAAC reaction, followed by radiolabeling of the NPs with  $^{111}\text{In}$  for monitoring the biodistribution of the administered NPs using SPECT/CT imaging. Alexa Fluor 488 was covalently conjugated to the nanocarrier for long-term biodistribution studies. In this work, we hypothesize that we can improve the efficacy of the anticancer therapy of the anti-angiogenic drug sorafenib by using PSi-based nanotheranostic systems. By iRGD-modification of the PSi NPs, we aimed for enhancing the nanoparticle tumor accumulation and retention when administered intravenously and intratumorally, respectively.

## 2. Materials and methods

### 2.1. Materials and cell culture

Dibenzocyclooctyne-PEG4-amine (DBCO-PEG4-amine) was purchased from Click Chemistry Tools (Scottsdale, USA). Azidoalanine-modified iRGD was purchased from GenicBio (China). 1,4,7,10-Tetraazacyclododecane-1,4,7-tris acetic acid-10-(azidopropyl-ethylacetamide) (Azido-mono-amide-DOTA) was purchased from Macrocyclics Inc (USA). Sorafenib was obtained from LC laboratories® (USA).  $^{111}\text{In}$  labeling was carried out with no-carrier-added  $^{111}\text{InCl}_3$  in 0.04 M HCl (370 MBq/mL, Mallinckrodt Medical B.V., The Netherlands). All the other chemicals were obtained

from Sigma–Aldrich (USA) and used as received, unless otherwise stated. Dulbecco's phosphate buffer saline (10× PBS), Hank's balanced salt solution (10× HBSS), Dulbecco's Modified Eagle's Medium (DMEM), fetal bovine serum (FBS), trypsin (2.5%), sodium pyruvate, nonessential amino acids (100 × NEAA), L-glutamine (100×), penicillin-streptomycin (100× PEST) were all purchased from HyClone (USA).

The highly metastatic prostate cancer cell PC3-MM2 was cultured in DMEM supplemented with 10% FBS, 1% NEAA, 1% L-glutamine, and 1% PEST (100 IU/mL) in 75 cm<sup>2</sup> flasks incubated at 37 °C in a humidified atmosphere (95%) and 5% CO<sub>2</sub>.

### 2.2. Multifunctional PSi NPs preparation

Undecylenic acid-modified thermally hydrocarbonized PSi (UnTHCPSi) NPs were prepared by electrochemical etching and wet-milling, as described elsewhere [43]. DBCO-PEG4-amine and Alexa Fluor 488 (Life Technologies, USA) were conjugated to UnTHCPSi NPs via N-hydroxysuccinimide (NHS) and 1-ethyl-3-(3-dimethylaminopropyl)-carbodiimide (EDC) coupling reaction. Briefly, 1 mg of UnTHCPSi NPs was mixed with 3 mg of NHS and 2 µL of EDC in 2 mL of 4-(2-hydroxyethyl)-1-piperazineethanesulfonic acid (HEPES, pH 5.5) buffer for 30 min. After that, 1 mg of DBCO-PEG4-amine and 10 µg of Alexa Fluor 488 were added to the reaction mixture, and the pH was adjusted to 7.8 with 1 M NaOH. After 1 h, the NPs were harvested by centrifugation (Sorvall RC 5B plus, Thermo Fisher Scientific, USA) at 10,000 g for 3 min and washed three times with 1 mL of dimethylformamide (DMF), water and ethanol (99.6%, Altia Corporation, Finland) to obtain Alexa Fluor 488-labeled and DBCO-modified PSi NPs (UnTHCPSi-Alexa488-DBCO).

Next, DOTA and iRGD were sequentially conjugated to UnTHCPSi-Alexa488-DBCO by the SPAAC reaction. First, the azido-mono-amide-DOTA (10 µg in DMF) was added to 1 mg of UnTHCPSi-Alexa488-DBCO (in Milli-Q water) for reaction at 37 °C for 30 min. The unreacted azido-mono-amide-DOTA was removed by washing with DMF, ethanol and Milli-Q water to obtain DOTA-labeled PSi NPs (UnTHCPSi-Alexa488-DBCO-DOTA). After that, 1 mg of azidoalanine-iRGD was added to the vial containing UnTHCPSi-Alexa488-DBCO-DOTA NPs. After the reaction at 37 °C for 1 h, the NPs were collected from the reaction mixture by centrifugation and washed with 50% (v/v) ethanol–water, water and ethanol to obtain iRGD-modified multifunctional PSi NPs (UnTHCPSi-Alexa488-DBCO-DOTA-iRGD).

For simplicity, below we have designated the prepared UnTHCPSi-Alexa488-DBCO-DOTA and UnTHCPSi-Alexa488-DBCO-DOTA-iRGD NPs as PSi and PSi-iRGD, respectively, unless otherwise stated.

### 2.3. Physicochemical characterization of the NPs

The porosity, pore volume and the specific surface area of the UnTHCPSi NPs were determined by N<sub>2</sub> sorption at −196 °C using TriStar 3000 (Micromeritics Inc., USA), as described in Supporting information. The qualitative analysis of the surface modification of the NPs was performed by Fourier transform infrared spectroscopy (FTIR) with a Vertex 70 spectrometer (Bruker Optics, USA) using a horizontal attenuated total reflectance (ATR) accessory (MIRacle, PIKE Technologies, USA). The spectra were recorded between 4000 and 650 cm<sup>−1</sup> with a 4 cm<sup>−1</sup> resolution. Hydrodynamic diameter (Z-average) and zeta (ζ)-potential measurements of the NPs were carried out using a Zetasizer Nano ZS (Malvern Instruments, UK) at 25 °C.

### 2.4. Cell viability studies

The cytotoxicity of the multifunctional NPs was evaluated by ATP-based cell viability kit, as described elsewhere [29]. Briefly, PC3-MM2 cells were seeded in 96-well plates at the density of  $1.5 \times 10^4$  cells/well and allowed to attach overnight. Then, the cell culture medium was replaced by 100 µL of medium (with or without 10% FBS) containing different concentrations of SF-loaded NPs (25, 50, 100, and 250 µg/mL). After 24 h incubation, the number of living cells was determined by the ATP-based cell viability kit (CellTiter-Glo® luminescent cell viability assay kit, Promega, USA), according to the manufacture's protocol. Each experiment was performed at least in triplicate. PC3-MM2 cells cultured in growth medium without NPs or with 1% of Triton X-100 served as positive and negative controls, respectively. The luminescence was measured with a Varioskan Flash fluorometer (Thermo Fisher Scientific, USA). The *in vitro* anti-proliferation effect of the SF-loaded PSi and PSi-iRGD NPs against the cancer cells growth was also evaluated using the same cell viability assay and conditions, as described above.

### 2.5. Drug loading and release

The poorly water-soluble antiangiogenic drug, sorafenib (SF), was loaded to the NPs for chemotherapy applications. The PSi and PSi-iRGD NPs were immersed in 50 mg/mL of SF dissolved in DMF solution with a ratio of 1 mg of NPs to 10 mg of drug in solution for drug loading studies. The loading degrees were determined by immersing 200 µg of the drug-loaded NPs to 1 mL of acetonitrile/water mixture (42:58, v/v) under vigorous stirring for 1 h and the supernatant was analyzed by high-performance liquid chromatography (HPLC) to determine the amount of SF loaded in the NPs. The dissolution profiles of SF from the PSi and PSi-iRGD NPs or free SF were performed at 37 ± 1 °C in sink conditions using a shaking-flask method with a shaking speed rate of 100 rpm. More detailed information on the assays is presented in Supporting Information.

## 2.6. $^{111}\text{In}$ -radiolabeling of the NPs

For  $^{111}\text{In}$  labeling of the NPs, 1.25–1.5 mg UnTHCPSi-Alexa488-DBCO-DOTA NPs were incubated with 178–309 MBq of  $^{111}\text{InCl}_3$  at 85 °C in 1.0 mL 0.1 M ammonium acetate buffer (pH 6.0). The peptide was conjugated to the NPs after  $^{111}\text{In}$  labeling to achieve a multifunctional nanocarrier system. Detailed description of the radiolabeling the NPs are presented in Supporting Information. The radiolabeled nanoparticles were stored at –20 °C in absolute ethanol. The nanoparticles were formulated in sterile 0.9% NaCl solution to a concentration of 83 MBq/mL before injection.

## 2.7. In vivo studies

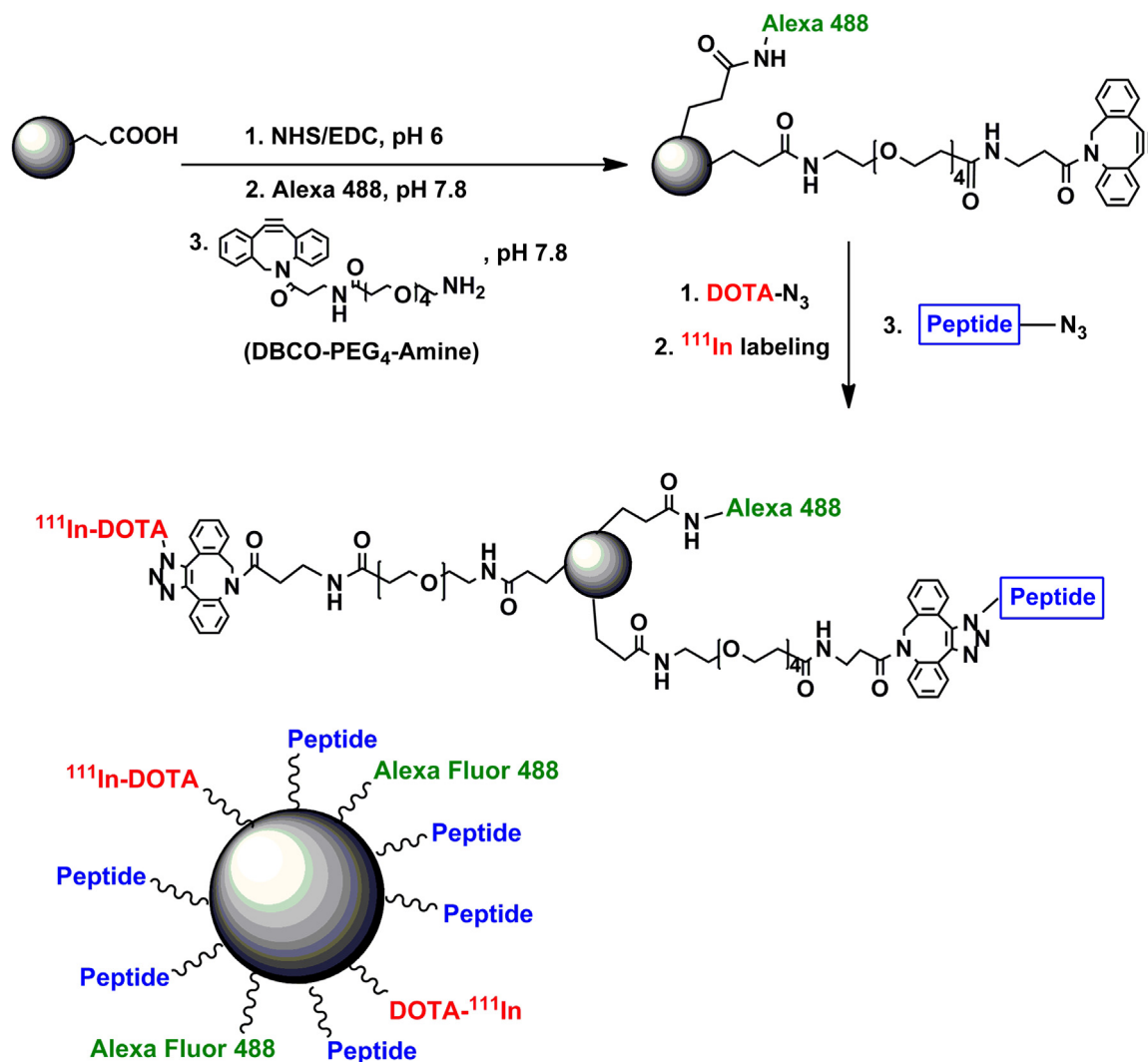
Animal experiments were performed in accordance to European Union and Finnish national legislation and guidelines for animal experimentation and were approved by the National Board for Animal Experimentation (license no. ESAVI/6735/04.10.03/2012). Male Hsd:NMRI-Foxn<sup>1nu/nu</sup> nude mice (6–8 weeks of age from Harlan) received bilateral subcutaneous injections of  $5 \times 10^6$  PC3-MM2 cells in 50  $\mu\text{L}$  DMEM into the flanks under isoflurane anesthesia (Attane Vet., ScanVet Animal Health, Finland) in air/oxygen carrier at 1.5% at 500 mL/min. The mice were randomized into the imaging and therapy study groups (the number of tumors used in each treatment group is provided in Supporting Information, Table S1) and tumors were allowed to develop for 8 days prior the studies. The study groups and experimental timelines for each are given in the subsequent sections. Nanoparticle and drug administrations were carried out under isoflurane anesthesia, as described

above. Intravenous injections were given in a volume of 120  $\mu\text{L}$  via a temporary catheter followed by a flush of the catheter with 0.1 mL of sterile 0.9% NaCl. Intratumoral administration was carried out with a U100 insulin syringe with a 30G needle in a volume of 50  $\mu\text{L}$ /tumor.

## 2.8. In vivo SPECT/CT imaging and biodistribution studies

The *in vivo* biodistribution of the developed multifunctional nanocarriers was assayed by using the small animal SPECT/CT system (Bioscan NanoSPECT/CT, Mediso, Hungary). The mice were dosed with  $^{111}\text{In}$ -radiolabeled PSi and PSi-iRGD NPs either intravenously or intratumorally and the whole-body SPECT/CT images were acquired under isoflurane anesthesia at 5 min after injection for 60 min (in dynamic scanning mode with 20 min frames and 16 projections at 90 s per projection), and again at 26 h after administration (16 projections and 225 s per projection). The CT images were acquired using 45 or 55 kV X-ray source, 500 ms exposure time in 180 projections, pitch 0.5 with an acquisition time of 5 min after the respective SPECT scan. All images were reconstructed with HiSPECT NG software (Scivis GmbH, Göttingen, Germany) and analyzed using *InVivo Scope* software (InvivoCRO LLC, USA).

After the last scan (27 h after administration), the mice were sacrificed by cervical dislocation under anesthesia and the samples of the blood, urine, liver, spleen, lung, heart, kidney, skeletal muscle, lymph node (inguinal), bone, and tumor were collected for independent radioactivity measurements using an automated  $\gamma$ -counter (Perkin Elmer Wizard 3, Perkin Elmer, USA). In addition, a 3  $\mu\text{L}$  blood sample for radioactivity measurement was obtained after the first SPECT/CT scan (at 65 min post-administration) by venipuncture of the saphenous vein.



**Scheme 1.** Scheme of the multifunctional nanocarrier preparation route. Alexa Fluor 488, DBCO, DOTA and iRGD were conjugated to UnTHCPSi NPs and are designated as PSi-iRGD and the NPs modified only with Alexa 488 and DOTA are designated as PSi.

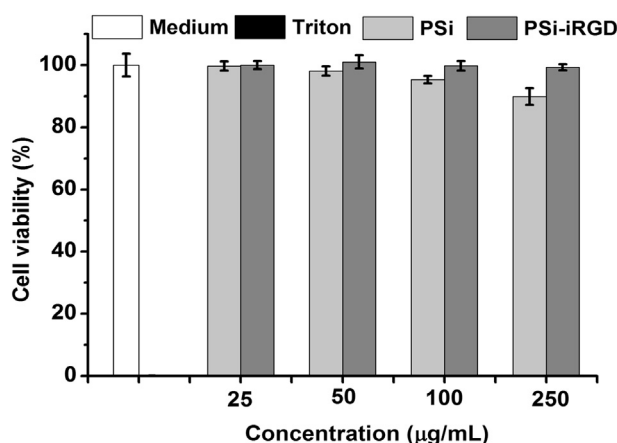


**Fig. 1.** *In vitro* cytotoxicity of the PSI and PSI-iRGD NPs was measured after 24 h incubation with PC3-MM2 cells at 37 °C. The cell viability was determined by using an ATP-based cell viability assay. Error bars represent mean  $\pm$  s.d. ( $n \geq 3$ ).

### 2.9. Sorafenib delivery and therapeutic efficacy

For the evaluation of the anticancer performance of the developed nanocarriers loaded with sorafenib (SF), the animals received two consecutive doses of SF-loaded NPs (3 mg/kg of SF) 24 h apart, on days 9 and 10 after the tumor inoculation. The median, minimum and maximum tumor sizes in each treatment group are given in supporting information (Table S2). On the first administration, the drug-loaded NPs were dosed together with  $^{111}\text{In}$ -radiolabeled particles analogously to the bio-distribution study to circumvent possible issues with the unforeseen radio-therapeutic effect of  $^{111}\text{In}$  on the tumor growth. Tumor development was monitored every other day after the tumor inoculation throughout the study with digital caliper measurements and the approximate tumor volume was determined with the formula  $V (\text{mm}^3) = [(\pi/6) \times (a \times b)^{3/2}]$ , where  $a$  and  $b$  are the values of the two perpendicular measurements of the tumor (length and width, respectively). The animals were euthanized after any of the diameters reached a maximum upper limit of 1.0 cm.

### 2.10. Immunofluorescence staining and histology

Immunofluorescence staining was used to determine the long-term bio-distribution of the multifunctional nanocarriers. When the tumor reached the upper growth limit, the mice were sacrificed and the liver, spleen, lung, kidney, heart, and tumors were collected and snap-frozen in liquid  $\text{N}_2$ . The tissues were sectioned to 5  $\mu\text{m}$  thickness on a cryostat microtome (Leica CM1950, Leica Biosystems, Germany) and the sections were thaw-mounted on SuperFrost Plus microscope slides (VWR Collection, Finland). The tumor samples were stained with rat anti-mouse CD31 antibody (BD Pharmingen, Germany) followed by Alexa Fluor 594-labeled anti-rat secondary antibody (BD Biosciences, USA) to visualize the blood vasculature. The cell surface expression of integrin  $\alpha_v\beta_3$  was visualized using a hamster anti-mouse CD61 antibody (Santa Cruz Biotechnology, USA) followed by Texas Red-labeled

anti-hamster secondary antibody (Santa Cruz Biotechnology, USA). The nuclei were counterstained with 4', 6-diamidino-2-phenylindole (DAPI, Vector Laboratories, USA). The stained sections of the tumors were imaged using a Leica SP5 inverted confocal microscope (Leica Microsystems, Germany) and the data was collected and analyzed by Leica LAS AF Lite software.

In order to analyze the biocompatibility of the multifunctional PSI and PSI-iRGD NPs and the tumor pathology after treatment, 5  $\mu\text{m}$  cryosections of the major organs and tumors were stained with hematoxylin and eosin (H&E). The slides were observed and photographed by optical microscope (Leica DM LB research microscope, Germany). Histopathological assessment of the tissue samples was also performed for the H&E stained sections by a veterinary pathologist.

### 2.11. Statistical analysis

Results of the assays were expressed as mean  $\pm$  standard deviation (s.d.) of at least three independent experiments. Student's  $t$ -test and a non-parametric Kruskal–Wallis test were used to evaluate the statistical significance, and the probability of  $*p < 0.05$  was considered statistically significant. The statistical analysis was carried out using Origin 8.6 (OriginLab Corp., Northampton, USA) and GraphPad Prism 6 (GraphPad Software, La Jolla, CA, USA) softwares.

## 3. Results and discussion

### 3.1. Multifunctional NPs preparation and physicochemical properties

The specific surface area, pore volume and average pore diameter of the plain UnTHCPSi NPs were  $251 \pm 4 \text{ m}^2/\text{g}$ ,  $0.66 \pm 0.01 \text{ cm}^3/\text{g}$ , and  $10.5 \pm 0.3 \text{ nm}$ , respectively. The  $\zeta$ -potential of the UnTHCPSi NPs obtained from the electrophoretic mobility measurements was  $-29.1 \text{ mV}$ .

The conjugation of the multifunctional moieties Alexa Fluor 488, DBCO, DOTA and iRGD to the UnTHCPSi NPs to achieve a multifunctional nanocarrier is depicted in Scheme 1. Each step of the surface modification was confirmed by FTIR (Fig. S1). The Alexa Fluor 488 and DBCO were conjugated to the UnTHCPSi NPs via amide linkage, which showed a typical amide vibration in the FTIR spectra (amide I and amide II at  $1650 \text{ cm}^{-1}$  and  $1550 \text{ cm}^{-1}$ , respectively) of the NPs after each reaction. The addition of ethylene glycol unit from the DBCO-PEG4-amine contributed to the C–H stretching, and the increased absorbance in the region of  $2800\text{--}2960 \text{ cm}^{-1}$ , indicating that DBCO was successfully conjugated to UnTHCPSi-Alexa488 NPs. After DOTA conjugation to the NPs, the peak of the carboxylic acid at  $1720 \text{ cm}^{-1}$  was strengthened. After iRGD conjugation to the NPs via SPAAC, the intensity of the amide peaks was increased, whereas the signal of both C–H stretch peak of alkane ( $2850\text{--}2960 \text{ cm}^{-1}$ ) and carboxylic acid peak ( $1720 \text{ cm}^{-1}$ ) was decreased. This was probably due to the

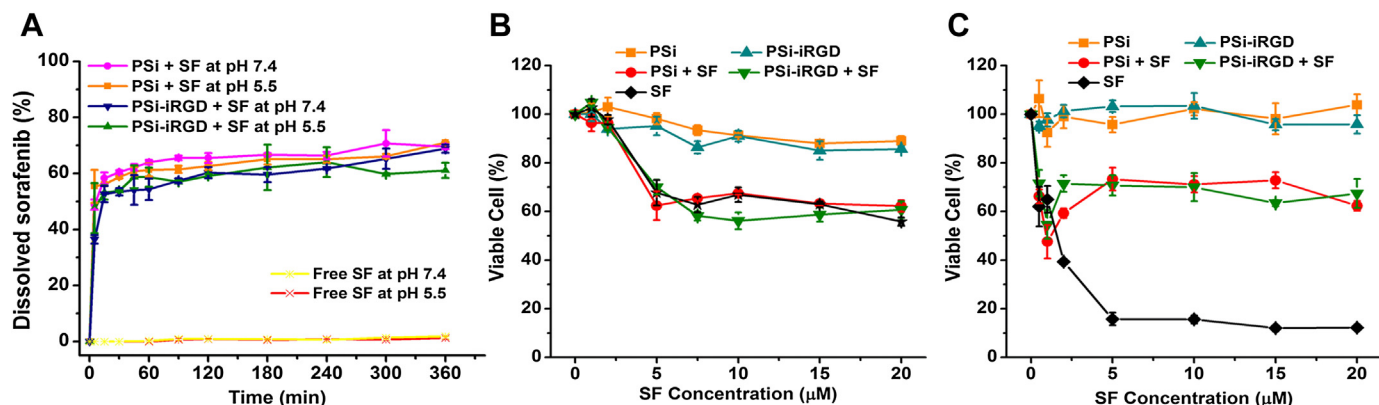


**Fig. 2.** Dissolution profiles of free SF, and SF loaded in PSI and PSI-iRGD nanoparticles, at pH 5.5 and pH 7.4 in the presence of 10% FBS (A), and effect of SF, loaded in PSI and PSI-iRGD nanoparticles, on cell viability with (B) or without (C) 10% FBS.



absorbance resulting from the presence of iRGD, indicating the successful synthesis of multifunctional NPs.

The sizes and  $\zeta$ -potentials of the NPs after each surface modification were measured by dynamic light scattering (DLS) and are summarized in Table S3. The particle size of UnTHCPSi-Alexa488-

DBCO was larger than UnTHCPSi-Alexa488-DOTA and UnTHCPSi-Alexa488-DOTA-iRGD NPs, probably due to the presence of the DBCO moiety (a hydrophobic compound) in the former ones, which may lead to partial NP aggregation. By introducing the hydrophilic moieties such as DOTA and iRGD, the PSi NPs became

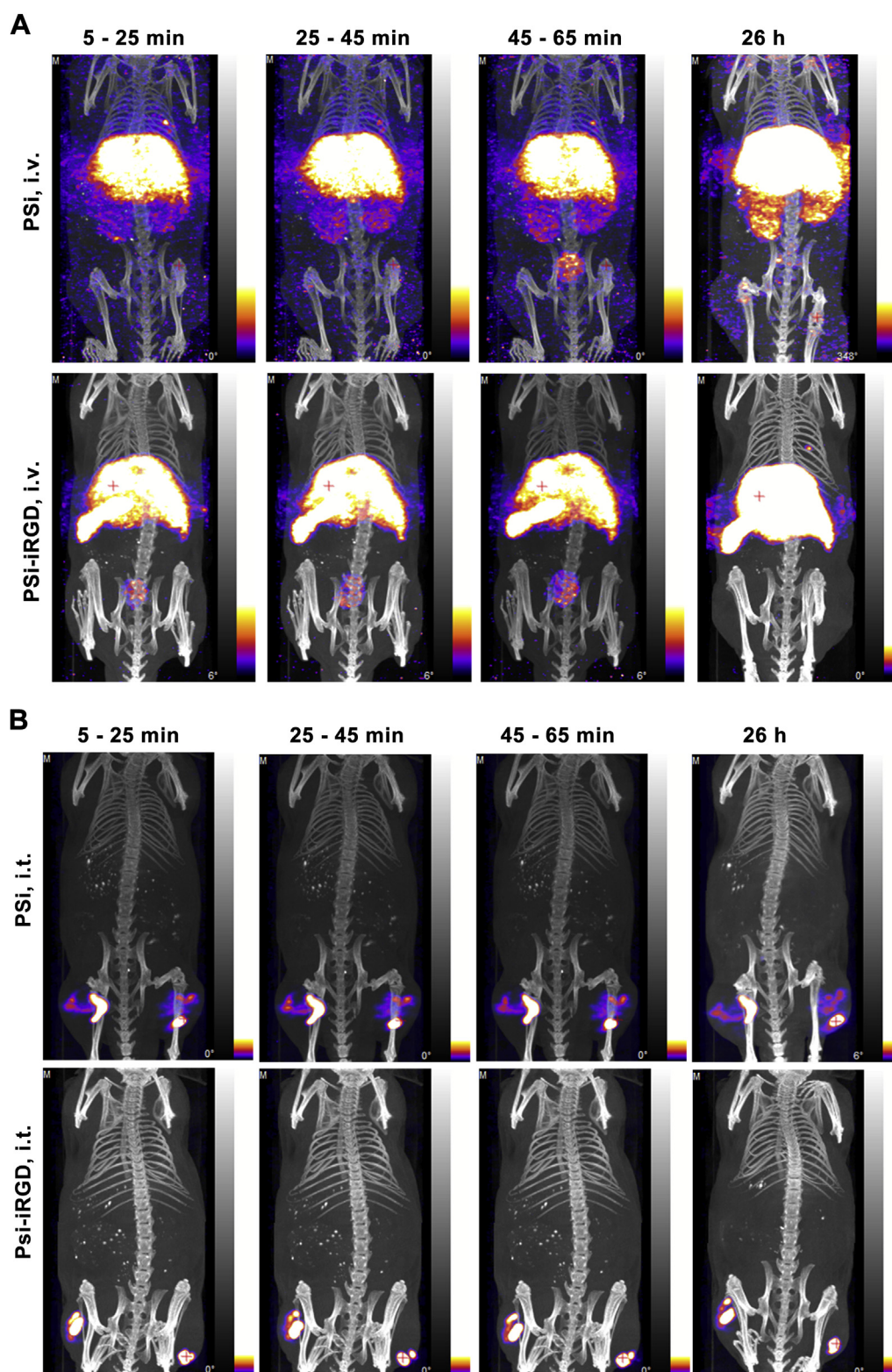


**Fig. 3.** Nano-SPECT/CT fused images of the whole mouse. Images were taken in a dynamic mode during 1 h at 5 min post-injection (p.i.) and at 26 h p.i. for PSi i.v. and PSi-iRGD i.v. (A), and PSi i.t. and PSi-iRGD i.t. (B) (i.v., intravenous; i.t., intratumoral).

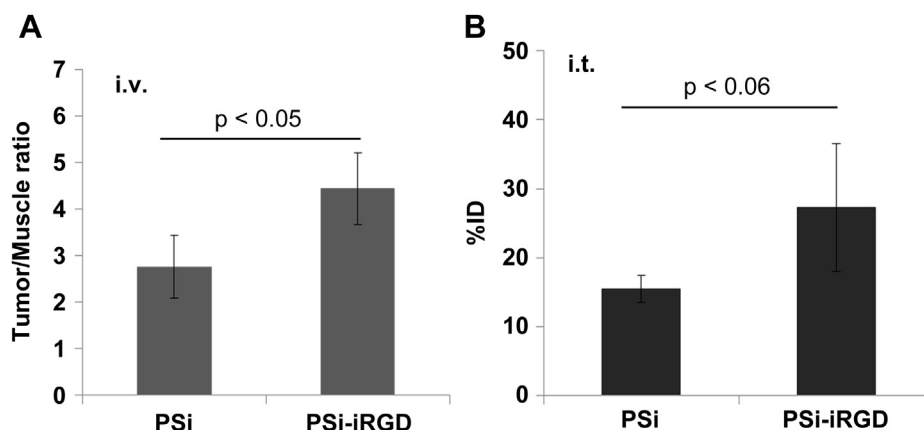


**Fig. 4.** Tumor accumulation of the PSi and PSi-iRGD NPs after i.v. administration (A) and tumor retention after i.t. administration (B) 27 h p.i. (i.v., intravenous; i.t., intratumoral).

better dispersed in the aqueous solution, and thus, smaller particle size and lower polydispersity index (Pdl) were observed for these NPs.

### 3.2. Radiolabeling of the multifunctional NPs

PSi and PSi-iRGD NPs were successfully labeled with  $^{111}\text{In}$  ( $t_{1/2} = 2.80$  d) by DOTA chelation. The decay-corrected radiochemical yields (RCY) from  $^{111}\text{InCl}_3$  were  $59.3 \pm 12.2\%$  and  $31.9 \pm 7.2\%$  for PSi and PSi-iRGD NPs, respectively. The lower RCY for the iRGD-modified particles might be due to the removal of weakly bound chelated- $^{111}\text{In}$  during the step of peptide conjugation to radio-labeled particles, which was further proved by SPECT/CT imaging (SPECT/CT imaging section). However, comparable specific activities,  $50.3 \pm 9.3$  MBq/mg and  $50.5 \pm 9.4$  MBq/mg, respectively, were attained for both particle types.

### 3.3. In vitro cytotoxicity of the NPs

The biocompatibility is the first prerequisite property of the NPs to be used for drug delivery applications. PSi based nanomaterials have been shown with good biocompatibility for biomedical applications [6]. The PC3-MM2 cells, a highly metastatic variant of the PC-3 prostate cancer cell line derived from a mouse liver metastasis, were selected for the *in vitro* and subsequent *in vivo* studies because they have been previously indicated to be responsive to antiangiogenic treatment [44]. The *in vitro* cytotoxicity of PSi and PSi-iRGD NPs was measured after 24 h incubation with the PC3-MM2 cells. No toxicity was observed with either of the prepared NPs *in vitro* (Fig. 1).

### 3.4. Drug loading, drug release and in vitro chemotherapy studies

The hydrophobic, antiangiogenic drug sorafenib (SF) was used as a model compound to test the multifunctional nanocarriers used for simultaneous chemotherapy drug delivery and *in vivo* imaging. SF has been used as a first-line anticancer medicine in the clinic [45,46]. However, its clinical application has been limited due to severe side effects and high variation between the patients caused by the poor water-solubility of SF [46–48]. The drug loading degree (the ratio of loaded SF mass relative to the total mass of drug-loaded NPs) was 28.2% and 27.0% for PSi and PSi-iRGD, respectively (Table S3). The iRGD-biofunctionalized NPs had a drug loading efficiency comparable to that of the PSi NPs.

SF is insoluble in water but avidly binds to plasma proteins which improves its dissolution and release from the PSi matrix [29]. The dissolution analysis of free SF and loaded SF from both PSi and

PSi-iRGD NPs was performed in buffer containing 10% FBS. SF loaded in either PSi or PSi-iRGD NPs reached 50–60% of SF dissolution in the first 15 min (Fig. 2A). Whereas free SF showed rather slow dissolution rate. Only about 0.89% (pH 5.5) and 0.94% (pH 7.4) of free SF was dissolved in the first 2 h. At 24 h, there was about 2.6% (pH 5.5) and 3.6% (pH 7.4) of free SF dissolved, and 5.1% (pH 5.5) and 8.7% (pH 7.4) after 168 h. Loading into both PSi and PSi-iRGD NPs significantly increased the dissolution rate of SF due to the nano-scale porous structure and the high surface area-to-volume ratio of the NPs [19,26].

The *in vitro* anticancer effect of SF, loaded in both PSi and PSi-iRGD NPs, was measured against PC3-MM2 cells using an ATP-based cell viability assay. SF alone was first dissolved in DMSO of 2 mM as a stock solution. The cell growth inhibition effect of SF, loaded in PSi and PSi-iRGD NPs, was performed in DMEM both with and without 10% FBS (Fig. 2B and C). In the presence of FBS, both free SF and loaded SF reached similar dose-dependent reduction in the cancer cell viability (Fig. 2B). This was probably due to the fast release of SF from the NPs to the growth medium in the presence of FBS. About 40% of cell death was achieved at the SF concentration of 5  $\mu\text{M}$ . Further increase in the SF concentration did not decrease the number of viable PC3-MM2 cells. It has been reported that PC3-MM2 cells treated by paclitaxel (Taxol<sup>®</sup>) retained the cell viability and the number of viable cells was increased until paclitaxel reached a concentration of 10  $\mu\text{M}$ , which caused cytotoxicity and induced about 40% of cell death [49]. Limited cytotoxicity of SF to PC3-MM2 might be due to the aggressive proliferative capability of the PC3-MM2 cells in the cell culture medium with 10% FBS. When the cell viability experiments were performed in absence of FBS (Fig. 2C), PC3-MM2 cells were successfully killed by SF at the concentrations exceeding 5  $\mu\text{M}$ . Conversely, SF loaded in both NPs achieved about 30% cell death, which stayed constant even after increasing the concentration of NPs loaded with SF. It has previously been reported that SF has extremely poor-water solubility in aqueous buffer without FBS [29]. The low efficiency on inhibiting the cell growth in the medium without FBS was likely due to the insolubility of the drug, and consequent limited release of SF from the nanocarriers in the absence of FBS *in vitro*.

### 3.5. SPECT/CT imaging and biodistribution of the multifunctional NPs

Mice bearing prostate cancer xenografts were used for the SPECT imaging and the *in vivo* biodistribution of  $^{111}\text{In}$ -labeled multifunctional PSi and PSi-iRGD NPs was determined after both intravenous and intratumoral administrations (Fig. 3). Both PSi and PSi-iRGD NPs accumulated mainly in the liver and spleen after



intravenous injection as anticipated (Fig. 3A). The comparison of  $\gamma$ -counting results between PSi-iRGD and PSi NPs at 27 h shows that the liver uptake was very similar for both NPs ( $27.8 \pm 2.1$  ID%/g vs.  $24.4 \pm 0.8$  ID%/g,  $p > 0.05$ ) and slightly higher yet statistically insignificant uptake of PSi-iRGD NPs by the spleen ( $70.8 \pm 43.8$  ID

%/g vs.  $20.6 \pm 15.3$  ID%/g,  $p > 0.05$ ) (Fig. S2). A similar phenomenon to peptide functionalized nanovectors has also been reported elsewhere [16]. There was no visible uptake of the NPs to the tumor after intravenous administration in SPECT/CT images. During the first hour, there was a minor radioactive signal observed in the

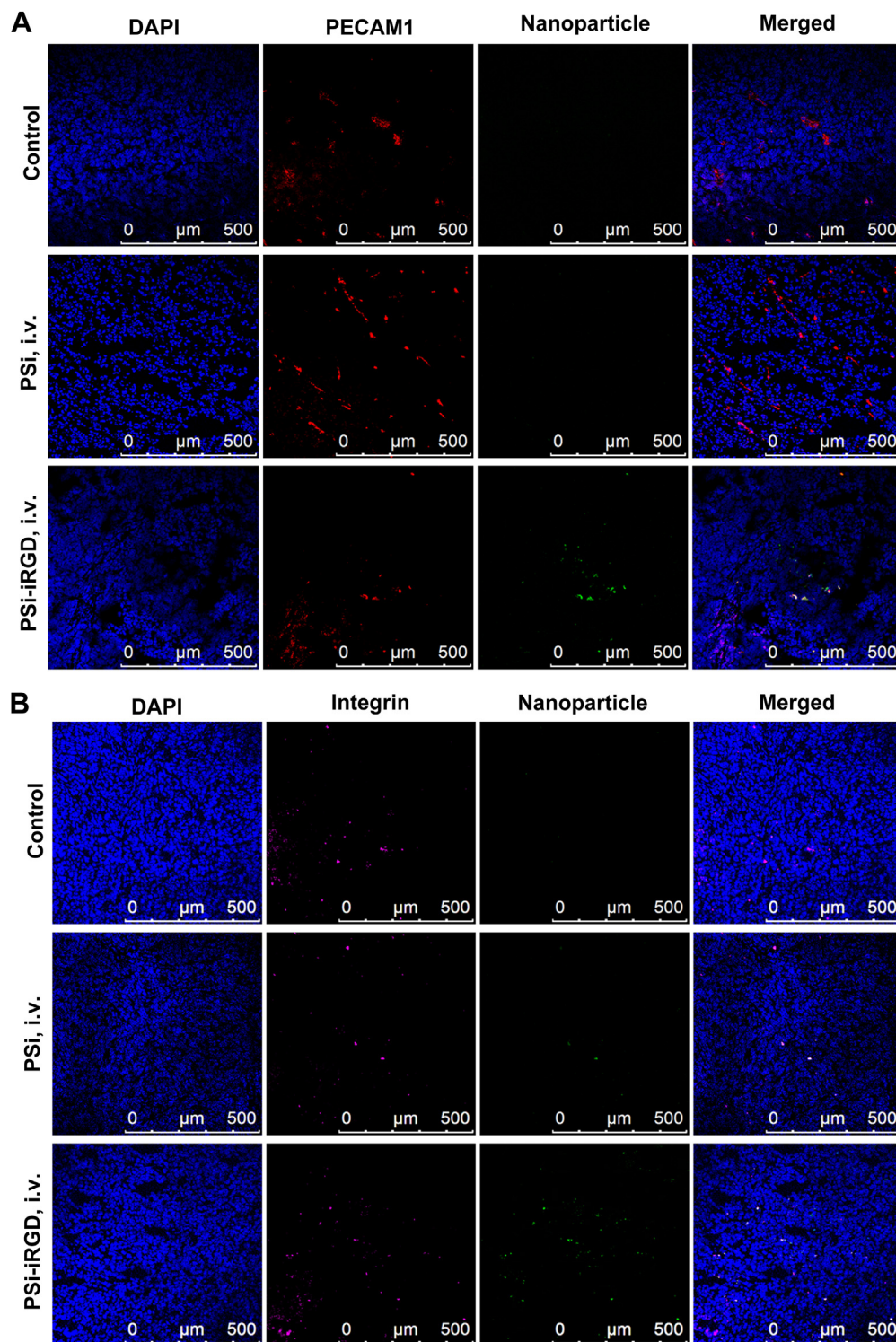


**Fig. 5.** Confocal images of immunofluorescence stained tumor sections from mice of i.v. (A and B) and i.t. (C and D) administered NPs. The images were taken from the middle of the tumor sections. Nuclei were stained with DAPI (blue), and CD31 (A and C) and integrin  $\beta 3$  (B and D) were separately visualized using antibodies pseudocolored here with red and magenta colors, respectively. The fluorescence signal of Alexa Fluor 488 attached to the NPs is shown in green. The last column shows the merged images (Scale bar: 500  $\mu$ m; i.v., intravenous; i.t., intratumoral). (For interpretation of the references to color in this figure legend, the reader is referred to the web version of this article.)

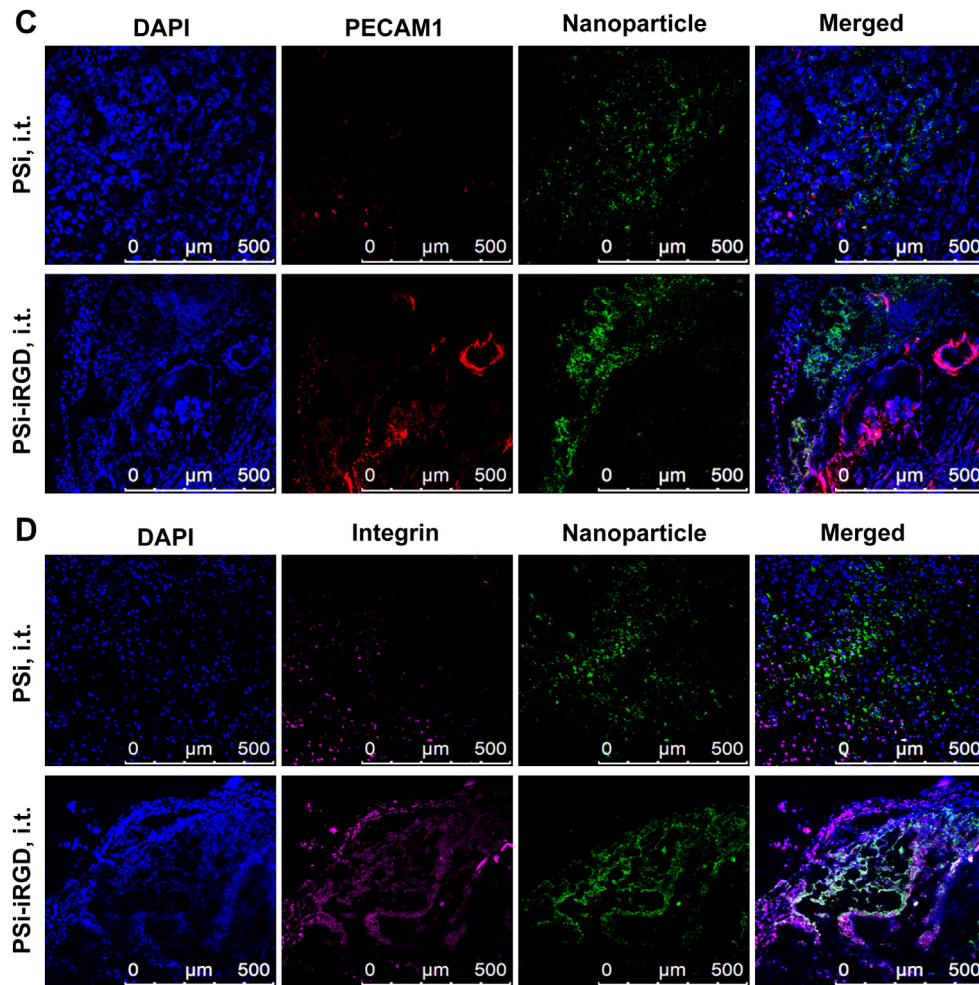


Fig. 5. (continued).

kidney for PSI NPs indicating detachment of small amounts of  $^{111}\text{In}$ , followed by an increase in radioactivity in the bladder. Detachment of the radiolabel from bare PSI NPs was more evident at the 26 h time point, when increased levels of radioactivity over the time were seen in the kidneys. On the other hand, yet minor radioactivity was observed in the bladder for the PSI-iRGD NP treated mice during the first 1 h; there was no visible radioactivity in the bladder or in the kidney of the PSI-iRGD NP treated mice at 26 h time point. This indicates that except the minor impurity of residual  $^{111}\text{In}$  left in the PSI-iRGD labeling, the  $^{111}\text{In}$  label in PSI-iRGD NPs was very stable. These results were further confirmed by the  $\gamma$ -counting radioactivity of the tissue samples (see the following section). After intratumoral administration, most of the PSI and PSI-iRGD NPs were retained in the tumor. For both NPs, the radioactivity was mainly found at the injection site in the tumor by SPECT/CT imaging up to 27 h, indicating that both NPs were retained in the tumor after intratumoral administration.

The radioactivity in the blood was measured at 65 min and 27 h post-injection (p.i.) (Fig. S3). After 65 min, less than 1.5 ID%/g of radioactivity was detected in the blood for both NPs, indicating fast clearance of the NPs from the circulation after the intravenous administration. As expected, the blood radioactivity continued to decrease further until 27 h ( $<0.3$  ID%/g) for both NPs. The observed slightly higher blood radioactivity levels of PSI NPs at 27 h p.i. are more likely originating from detached radiolabel than circulating NPs, as the radioactivity in the kidney was also seen, indicating excretion of free  $^{111}\text{In}$ .

The intravenously administered iRGD-modified NPs had higher tumor specific accumulation compared to the PSI NPs, as judged from the 4.4 vs. 2.7 tumor-to-muscle ratios of the radioactivity (ID %/g), for PSI-iRGD and PSI, respectively (Fig. 4A). iRGD surface modification to the nanocarriers can increase the tumor accumulation of the nanocarriers [39,50]. Intratumoral administration of nanocarriers can result in much higher tumor-to-tissue ratio of the nanomaterials compared to intravenous administration. However, the elimination of the carriers from the tumor is still relatively fast and dependent on the properties of the nanocarriers [42]. In our case, after intratumoral administration, PSI-iRGD NPs showed higher tumor retention compared to PSI NPs (Fig. 4B), but the difference between the two particle types was not statistically significant. Therefore, it is possible that the iRGD modification aided the PSI-iRGD NPs to interact with the tumor cells, and thus, improving the retention of the nanocarrier inside the tumor by slowing down the elimination from the tumor microenvironment.

After the 26 h time point SPECT scan, the mice were sacrificed and the major organs were collected to obtain an independent quantitative determination of the percentage of the injected dose retained in the organs by  $\gamma$ -counting (Fig. S2). The  $\gamma$ -counting results of each organ samples were consistent with SPECT/CT imaging. In the case of the intravenous administration, both PSI and PSI-iRGD NPs were mainly taken up by the liver and spleen 27 h p.i., with minor radioactivity distributed in the lung, heart, kidney, skeletal muscle, lymph node, bone, and urine. There was



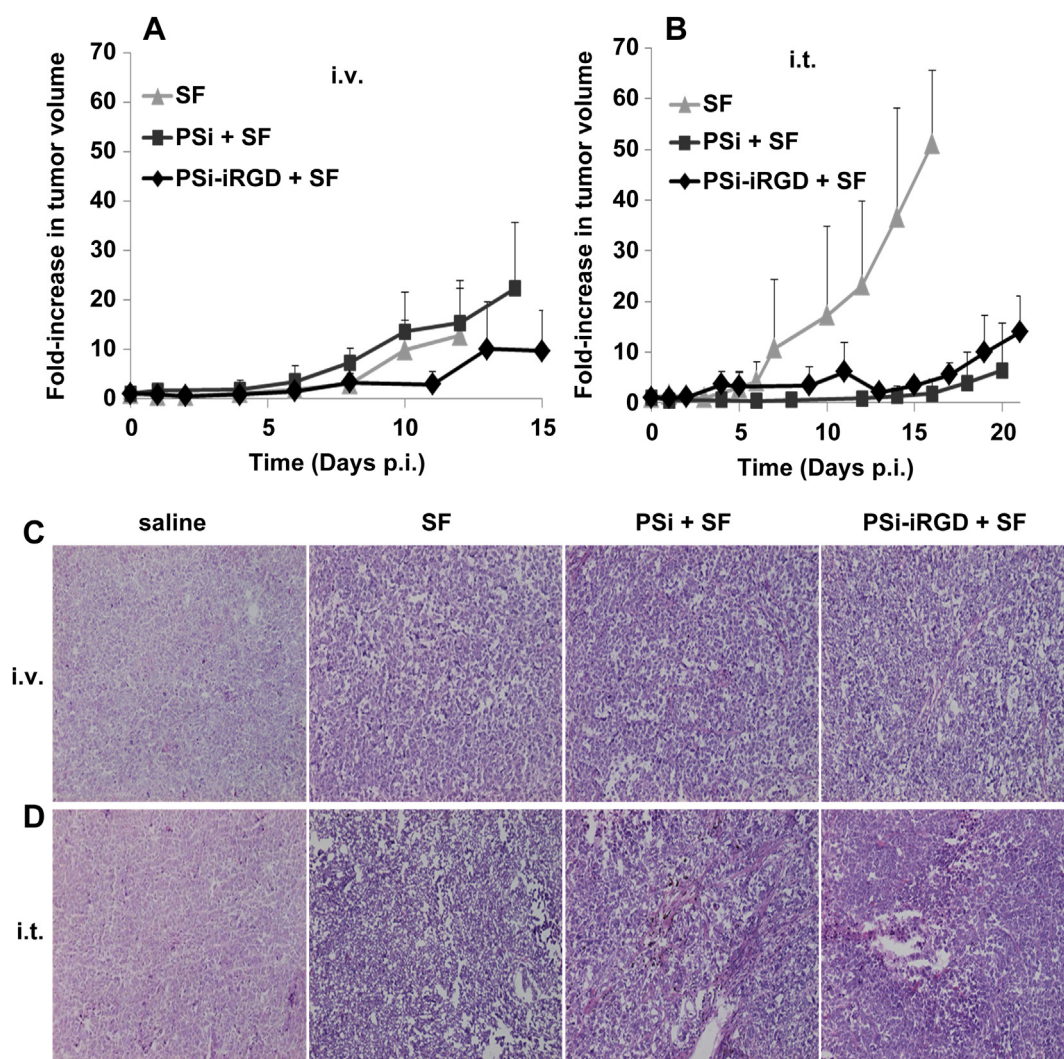


**Fig. 6.** Inhibition of tumor growth by the SF (A and B) and H&E staining tissue tumor sections (C and D) after different treatments (saline, SF, PSi + SF and PSi-iRGD + SF) of the nude mice bearing PC3-MM2 prostate cancer xenografts. Data are represented as mean  $\pm$  s.d. ( $n = 4-6$ ). Delivery of SF induced necrosis to the tumor tissues (i.v., intravenous; i.t., intratumoral; p.i., post-injection). The statistical differences are PSi-iRGD + SF vs. PSi + SF vs. SF,  $p = 0.3238$  (intravenous administration route, Kruskal–Wallis test) and  $p = 0.0107$  (intratumoral administration route, Kruskal–Wallis test).

significantly higher radioactivity in the kidney of mice treated by PSi NPs than that of PSi-iRGD NPs, which met the results from the SPECT/CT images. In the case of intratumoral administration, lower radioactivity levels were observed in all the organs of the mice treated with PSi-iRGD NPs than that when treated with PSi NPs, which was complementary to the radioactivity that was retained in the tumor. This corroborated the results that the iRGD modification can possibly enhance the retention of the PSi NPs in the tumor.

### 3.6. Histological analysis

Long-term tissue biodistribution of PSi and PSi-iRGD NPs were assessed by immunofluorescence staining of the tumor and tissue samples. Anti-CD31 and anti-CD61 antibodies were employed to visualize the blood vasculature and the RGD peptide receptor, integrin  $\beta_3$ , respectively. Integrin  $\beta_3$  is expressed by both endothelial cells and tumor cells. iRGD has been reported as one of the derivatives of RGD, which has high affinity to integrin  $\alpha_v\beta_3$ , and is able to penetrate deep into the tumor [38]. After intravenous administration both PSi and PSi-iRGD NPs accumulated onto the surface of the tumors and colocalized together with blood

vasculature likely due to the EPR effect (Fig. S4). However, only PSi-iRGD NPs were found in the middle of the tissue tumor sections (Fig. 5), corroborating the report that the iRGD-functionalization of NPs promotes the NPs penetrating into the tumor stroma [38]. In the case of intratumoral administration, a concentrated mass of both PSi and PSi-iRGD NPs were seen at the injection site in the tumor section which is in agreement with the SPECT/CT images and the  $\gamma$ -counting results supporting the observation that high amounts of the nanoparticles were retained in the tumor after localized delivery.

### 3.7. Anticancer effect of the multifunctional NPs

The antitumor effect of the multifunctional NPs loaded with SF *in vivo* was assessed. The tumor growth was monitored every other day after the tumor inoculation with digital caliper measurements of the tumor size. The tumor growth curve shows the ratio of the tumor size after treatment compared to the initial tumor size before treatment, and the tumor growth in the different treatment groups over time is presented in Fig. 6A and 6B. After two cycles of intravenous administration 24 h apart, both SF loaded NPs (PSi-SF and PSi-iRGD-SF corresponding to 3 mg/kg of SF) affected the

tumor growth similarly as the free SF (Fig. 6A). This is probably due to the fast release of SF from the PSi matrix into the blood after intravenous administration. After intratumoral administration of two consecutive injections 24 h apart, SF loaded in PSi and PSi-iRGD NPs inhibited tumor growth significantly better than the free SF (Fig. 6B). This is likely an indication of sustained release of the SF from the nanocarrier in the tumor microenvironment over time, probably due to the limited dissolution rate of the drug under this condition. Furthermore, the deposit of NPs after i.t. administration was still visible after >20 days in animals used in the therapy study, indicating that such sustained release was feasible under the experimental conditions. The intratumorally administered SF showed negligible tumor suppression probably due to the rapid elimination of the small drug molecules from the tumor [40,42]. The antitumor effect was also assessed via H&E staining of the tumor sections (Fig. 6C and D). The tumor sections from mice treated with SF loaded in both PSi and PSi-iRGD showed comparable necrotic areas for the same administration route of the free SF. The necrotic areas in the case of intravenous administration were smaller but more evenly distributed in the tumor section than in the case of intratumoral administration.

H&E stained samples of the major tissue sections were also accessed to evaluate the long term biocompatibility of the multifunctional PSi and PSi-iRGD NPs (Fig. S5). The morphology of the liver, spleen, lung, kidney, and heart revealed that there were no signs of tissue necrosis, fibrosis, or inflammation at all the treatment groups both after intravenous and intratumoral administration.

#### 4. Conclusion

We have successfully prepared a dual-labeled multifunctional PSi nanosystem for cancer theranostic applications. UnTHCPSi nanoparticles were modified to incorporate an  $^{111}\text{In}$  radiolabel, fluorescent Alexa Fluor 488 dye, and a tumor-homing iRGD peptide, allowing for visualization of the nanocarrier's biodistribution *in vivo* with SPECT/CT together with its tissue-level localization *ex vivo* with fluorescence microscopy, and integrin targeting in a mouse xenograft model of prostate cancer. Our multimodal imaging approach demonstrates how different aspects of the theranostic nanosystem performance can be assessed using a single imaging probe with defined physicochemical characteristics at both cellular and whole organism levels. After intravenous administration, the iRGD modification resulted in higher tumor-to-background radioactivity in the NPs uptake and NPs tumor penetration by immunofluorescence staining, illustrating that targeting was achieved. However, both the non-targeted PSi and the iRGD-targeted PSi NPs were subject to the rapid recognition and removal from the circulation by cells of the reticuloendothelial system. This needs to be improved by further tailoring of the surface properties of the developed nanosystem. After local intratumoral delivery the NPs were retained in the tumor for extended periods of time. This was translated to efficient PC3-MM2 prostate cancer xenograft growth suppression when sorafenib was delivered by the NPs intratumorally. H&E staining results showed a good biocompatibility of the multifunctional PSi nanocarrier. Overall, we have shown that PSi nanomaterials can be functionalized with multiple moieties for imaging and targeting drug delivery without impairing their unique drug delivery properties, rendering the presented multimodal nanosystem a promising one for the future development of nanotheranostic PSi systems for cancer diagnostics and treatment.

#### Competing interests

The authors have no competing interests.

#### Acknowledgments

Dr. H.A. Santos acknowledges the University of Helsinki Research Funds, the Biocentrum Helsinki, the Academy of Finland (decision nos. 252215 and 256394), and the European Research Council under the European Union's Seventh Framework Programme (FP/2007–2013) grant no. 310892 for financial support. Dr. A.J. Airaksinen acknowledges the Academy of Finland (decision nos. 136805 and 272908). Dr. P. Laakkonen acknowledges the financial support from the Finnish Cancer Organizations and Finnish Cancer Institute. Prof. Akseli Hemminki (Faculty of Medicine, Biomedicum Helsinki, University of Helsinki, Finland) is acknowledged for generously providing the PC3-MM2 cells. Marjo Vaha (Division of Pharmacology and Pharmacotherapy, Faculty of Pharmacy, University of Helsinki) is acknowledged for technical support with the SPECT/CT measurements. Pathologist Dr. Jere Lindén (Finnish Centre for Laboratory Animal Pathology, Department of Veterinary Biosciences, Faculty of Veterinary Medicine, University of Helsinki, Finland) is acknowledged for technical support with the histopathological assessment of the tissue samples.

#### Appendix A. Supplementary data

Supplementary data related to this article can be found at <http://dx.doi.org/10.1016/j.biomaterials.2015.01.008>.

#### References

- [1] Ferlay J, Steliarova-Foucher E, Lortet-Tieulent J, Rosso S, Coebergh JWW, Comber H, et al. Cancer incidence and mortality patterns in Europe: estimates for 40 countries in 2012. *Eur J Cancer* 2013;49:1374–403.
- [2] Edwards BK, Noone A-M, Mariotto AB, Simard EP, Boscoe FP, Henley SJ, et al. Annual report to the nation on the status of cancer, 1975–2010, featuring prevalence of comorbidity and impact on survival among persons with lung, colorectal, breast, or prostate cancer. *Cancer* 2014;120:1290–314.
- [3] Ruoslahti E, Bhatia SN, Sailor MJ. Targeting of drugs and nanoparticles to tumors. *J Cell Biol* 2010;188:759–68.
- [4] Ruoslahti E. Specialization of tumour vasculature. *Nat Rev Cancer* 2002;2:83–90.
- [5] Ryu JH, Lee S, Son S, Kim SH, Leary JF, Choi K, et al. Theranostic nanoparticles for future personalized medicine. *J Control Release* 2014;190:477–84.
- [6] Bimbo LM, Sarparanta M, Santos HA, Airaksinen AJ, Mäkilä E, Laakkonen T, et al. Biocompatibility of thermally hydrocarbonized porous silicon nanoparticles and their biodistribution in rats. *ACS Nano* 2010;4:3023–32.
- [7] Hong H, Chen F, Zhang Y, Cai W. New radiotracers for imaging of vascular targets in angiogenesis-related diseases. *Adv Drug Deliv Rev* 2014;76:2–20.
- [8] Cutler CS, Hennkens HM, Sisay N, Huclier-Markai S, Jurisson SS. Radiometals for combined imaging and therapy. *Chem Rev* 2013;113:858–83.
- [9] Xie J, Lee S, Chen X. Nanoparticle-based theranostic agents. *Adv Drug Deliv Rev* 2010;62:1064–79.
- [10] Couvreur P. Nanoparticles in drug delivery: past, present and future. *Adv Drug Deliv Rev* 2013;65:21–3.
- [11] Bai F, Wang C, Lu Q, Zhao M, Ban FQ, Yu DH, et al. Nanoparticle-mediated drug delivery to tumor neovasculature to combat P-gp expressing multidrug resistant cancer. *Biomaterials* 2013;34:6163–74.
- [12] Bigini P, Previdi S, Casarin E, Silvestri D, Violatto MB, Facchin S, et al. *In vivo* fate of avidin-nucleic acid nanoassemblies as multifunctional diagnostic tools. *ACS Nano* 2014;8:175–87.
- [13] Chen Q, Wang C, Cheng L, He W, Cheng Z, Liu Z. Protein modified upconversion nanoparticles for imaging-guided combined photothermal and photodynamic therapy. *Biomaterials* 2014;35:2915–23.
- [14] Li J, He Y, Sun W, Luo Y, Cai H, Pan Y, et al. Hyaluronic acid-modified hydrothermally synthesized iron oxide nanoparticles for targeted tumor MR imaging. *Biomaterials* 2014;35:3666–77.
- [15] Zhang H, Liu D, Shahbazi MA, Mäkilä E, Herranz-Blanco B, Salonen J, et al. Fabrication of a multifunctional nano-in-micro drug delivery platform by microfluidic templated encapsulation of porous silicon in polymer matrix. *Adv Mater* 2014;26:4497–503.
- [16] Kinnari PJ, Hyvonen ML, Mäkilä EM, Kaasalainen MH, Rivinoja A, Salonen JJ, et al. Tumor homing peptide-functionalized porous silicon nanovectors for cancer therapy. *Biomaterials* 2013;34:9134–41.
- [17] Liu D, Zhang H, Herranz-Blanco B, Mäkilä E, Lehto VP, Salonen J, et al. Microfluidic assembly of monodisperse multistage pH-responsive polymer/porous silicon composites for precisely controlled multi-drug delivery. *Small* 2014;10:2029–38.

- [18] Shahbazi MA, Hamidi M, Mäkilä EM, Zhang H, Almeida PV, Kaasalainen M, et al. The mechanisms of surface chemistry effects of mesoporous silicon nanoparticles on immunotoxicity and biocompatibility. *Biomaterials* 2013;34:7776–89.
- [19] Bimbo LM, Denisova OV, Mäkilä E, Kaasalainen M, De Brabander JK, Hirvonen J, et al. Inhibition of influenza A virus infection in vitro by saliphenylhalamide-loaded porous silicon nanoparticles. *ACS Nano* 2013;7:6884–93.
- [20] Bimbo LM, Mäkilä E, Raula J, Laaksonen T, Laaksonen P, Strommer K, et al. Functional hydrophobin-coating of thermally hydrocarbonized porous silicon microparticles. *Biomaterials* 2011;32:9089–99.
- [21] Liu D, Bimbo LM, Mäkilä E, Villanova F, Kaasalainen M, Herranz-Blanco B, et al. Co-delivery of a hydrophobic small molecule and a hydrophilic peptide by porous silicon nanoparticles. *J Control Release* 2013;170:268–78.
- [22] Sarparanta MP, Bimbo LM, Mäkilä EM, Salonen JJ, Laaksonen PH, Helariutta AM, et al. The mucoadhesive and gastroretentive properties of hydrophobin-coated porous silicon nanoparticle oral drug delivery systems. *Biomaterials* 2012;33:3353–62.
- [23] Santos HA, Riikonen J, Salonen J, Mäkilä E, Heikkilä T, Laaksonen T, et al. In vitro cytotoxicity of porous silicon microparticles: effect of the particle concentration, surface chemistry and size. *Acta Biomater* 2010;6:2721–31.
- [24] Rytönen J, Miettinen R, Kaasalainen M, Lehto V-P, Salonen J, Näränen A. Functionalization of mesoporous silicon nanoparticles for targeting and bio-imaging purposes. *J Nanomater* 2012;2012:896562.
- [25] Kaasalainen M, Mäkilä E, Riikonen J, Kovalainen M, Järvinen K, Herzig KH, et al. Effect of isotonic solutions and peptide adsorption on zeta potential of porous silicon nanoparticle drug delivery formulations. *Int J Pharm* 2012;431:230–6.
- [26] Salonen J, Laitinen L, Kaukonen AM, Tuura J, Björkqvist M, Heikkilä T, et al. Mesoporous silicon microparticles for oral drug delivery: loading and release of five model drugs. *J Control Release* 2005;108:362–74.
- [27] Santos HA, Bimbo LM, Lehto VP, Airaksinen AJ, Salonen J, Hirvonen J. Multifunctional porous silicon for therapeutic drug delivery and imaging. *Curr Drug Discov Technol* 2011;8:228–49.
- [28] Jarvis KL, Barnes TJ, Prestidge CA. Surface chemical modification to control molecular interactions with porous silicon. *J Colloid Interface Sci* 2011;363:327–33.
- [29] Wang CF, Mäkilä EM, Kaasalainen MH, Liu D, Sarparanta MP, Airaksinen AJ, et al. Copper-free azide-alkyne cycloaddition of targeting peptides to porous silicon nanoparticles for intracellular drug uptake. *Biomaterials* 2014;35:1257–66.
- [30] Sarparanta M, Mäkilä E, Heikkilä T, Salonen J, Kukk E, Lehto VP, et al.  $^{18}\text{F}$ -labeled modified porous silicon particles for investigation of drug delivery carrier distribution in vivo with positron emission tomography. *Mol Pharmacol* 2011;8:1799–806.
- [31] Liu X, Chen Y, Li H, Huang N, Jin Q, Ren K, et al. Enhanced retention and cellular uptake of nanoparticles in tumors by controlling their aggregation behavior. *ACS Nano* 2013;7:6244–57.
- [32] Lallana E, Sousa-Hervas A, Fernandez-Trillo F, Riguera R, Fernandez-Megia E. Click chemistry for drug delivery nanosystems. *Pharm Res* 2012;29:1–34.
- [33] Jewett JC, Bertozzi CR. Cu-free click cycloaddition reactions in chemical biology. *Chem Soc Rev* 2010;39:1272–9.
- [34] Sawoo S, Dutta P, Chakraborty A, Mukhopadhyay R, Bouloussa O, Sarkar A. A new bio-active surface for protein immobilisation via copper-free 'click' between azido SAM and alkynyl Fischer carbene complex. *Chem Commun* 2008;7:5957–9.
- [35] Manova RK, Pujari SP, Weijers CA, Zuilhof H, van Beek TA. Copper-free click biofunctionalization of silicon nitride surfaces via strain-promoted alkyne-azide cycloaddition reactions. *Langmuir* 2012;28:8651–63.
- [36] Lee DE, Na JH, Lee S, Kang CM, Kim HN, Han SJ, et al. Facile method to radiolabel glycol chitosan nanoparticles with Cu via copper-free click chemistry for microPET imaging. *Mol Pharmacol* 2013;10:2190–8.
- [37] Al-Jamal KT, Nunes A, Methven L, Ali-Boucetta H, Li S, Toma FM, et al. Degree of chemical functionalization of carbon nanotubes determines tissue distribution and excretion profile. *Angew Chem Int Ed Engl* 2012;51:6389–93.
- [38] Sugahara KN, Teesalu T, Karmali PP, Kotamraju VR, Agemy L, Girard OM, et al. Tissue-penetrating delivery of compounds and nanoparticles into tumors. *Cancer Cell* 2009;16:510–20.
- [39] Sugahara KN, Teesalu T, Karmali PP, Kotamraju VR, Agemy L, Greenwald DR, et al. Coadministration of a tumor-penetrating peptide enhances the efficacy of cancer drugs. *Science* 2010;328:1031–5.
- [40] Han HD, Byeon Y, Jeon HN, Shin BC. Enhanced localization of anticancer drug in tumor tissue using polyethylenimine-conjugated cationic liposomes. *Nanoscale Res Lett* 2014;9:9–209.
- [41] Nichols JW, Bae YH. EPR: evidence and fallacy. *J Control Release* 2014;190C:451–64.
- [42] Lammers T, Peschke P, Kuhnlein R, Subr V, Ulbrich K, Huber P, et al. Effect of intratumoral injection on the biodistribution and the therapeutic potential of HPMA copolymer-based drug delivery systems. *Neoplasia* 2006;8:788–95.
- [43] Kovalainen M, Mönkäre J, Kaasalainen M, Riikonen J, Lehto VP, Salonen J, et al. Development of porous silicon nanocarriers for parenteral peptide delivery. *Mol Pharmacol* 2013;10:353–9.
- [44] Huang SF, Kim SJ, Lee AT, Karashima T, Bucana C, Kedar D, et al. Inhibition of growth and metastasis of orthotopic human prostate cancer in athymic mice by combination therapy with pegylated interferon- $\alpha$ -2b and docetaxel. *Cancer Res* 2002;62:5720–6.
- [45] Awada A, Hendlitz A, Gil T, Bartholomeus S, Mano M, de Valeriola D, et al. Phase I safety and pharmacokinetics of BAY 43-9006 administered for 21 days on/7 days off in patients with advanced, refractory solid tumours. *Br J Cancer* 2005;92:1855–61.
- [46] Ravandi F, Cortes JE, Jones D, Faderl S, Garcia-Manero G, Konopleva MY, et al. Phase I/II study of combination therapy with sorafenib, idarubicin, and cytarabine in younger patients with acute myeloid leukemia. *J Clin Oncol* 2010;28:1856–62.
- [47] Jain L, Woo S, Gardner ER, Dahut WL, Kohn EC, Kummar S, et al. Population pharmacokinetic analysis of sorafenib in patients with solid tumours. *Br J Clin Pharmacol* 2011;72:294–305.
- [48] Boudou-Rouquette P, Narjoz C, Golmard JL, Thomas-Schoemann A, Mir O, Taieb F, et al. Early sorafenib-induced toxicity is associated with drug exposure and UGT1A9 genetic polymorphism in patients with solid tumors: a preliminary study. *PLoS One* 2012;7: e42875.
- [49] Botchkina GI, Zuniga ES, Rowehl RH, Park R, Bhalla R, Bialkowska AB, et al. Prostate cancer stem cell-targeted efficacy of a new-generation taxoid, SBT-1214 and novel polyenolic zinc-binding curcuminoid, CMC2.24. *PLoS One* 2013;8: e69884.
- [50] Su S, Wang H, Liu X, Wu Y, Nie G. iRGD-coupled responsive fluorescent nanogel for targeted drug delivery. *Biomaterials* 2013;34:3523–33.